PCCP

PAPER

View Article Online
View Journal | View Issue

Cite this: *Phys. Chem. Chem. Phys.*, 2015, **17**, 6076

The effect of TiO_2 surface on the electron injection efficiency in PbS quantum dot solar cells: a first-principles study†

Jon M. Azpiroz,*[ab] Jesus M. Ugalde,[a] Lioz Etgar,[c] Ivan Infante[ad] and Filippo De Angelis[b]

Received 29th October 2014,
Accepted 13th January 2015

DOI: 10.1039/c4cp04976d

www.rsc.org/pccp

We present a density functional theory (DFT) study aimed at understanding the injection and recombination processes that occur at the interface between PbS QDs and TiO_2 oxide nanoparticles with different morphologies. The calculated injection rates fall in the picosecond timescale in good agreement with the experiments. In addition, our simulations show that the (101) facet of TiO_2 more favourably accommodates the QD, resulting in stronger electronic couplings and faster electron injections than the (001) surfaces. Despite this, the (101) slab is also more prone to faster electron recombination with the valence band of the QD, which can lead to overall lower injection efficiencies than the (001) surface.

Introduction

In the past few decades, solar energy has emerged as an environmentally clean, efficient, cost-effective, renewable, and sustainable alternative to solid fuels. In this context, dye sensitized solar cells (DSSC) are embodying a significant leap forward to efficient light conversion at low cost.[1] DSSCs consist of a mesoporous wide gap oxide layer, usually TiO_2 or ZnO, grafted with a monolayer of sensitizing dye, which absorbs the solar radiation and injects the photogenerated electrons into the manifold of unoccupied states (conduction band or CB) of the oxide.[2] These electrons are then collected on an external load, while holes on the dyes are scavenged by an electrolyte/polymer and transported to the cathode where they close the circuit.

More recently, semiconductor quantum dots (QDs) have gained a lot of attention as efficient light harvesters due to their attractive properties.[3,4] QDs present high extinction coefficients and large dipole moments, and their absorption spectrum can be tuned by changing their size and morphology. In addition, QDs provide the opportunity to increase solar cell photocurrent by either extracting hot carriers or taking advantage of the multiple exciton generation (MEG) phenomenon, which can potentially overcome the Shockley–Queisser limit of 33% power conversion efficiency (PCE).[5] Along with these outstanding optoelectronic properties, QD nanocrystals are characterized by versatile and low-cost synthetic routes, and unmatched photostability that make them amenable for photovoltaic applications.

PbS QD nanocrystals, which belong to the IV–VI group, are among the most popular semiconductor QDs. They present a relatively large Bohr radius (18 nm) that allows tuning of their band-gap in the 0.5 to 5.5 eV range (*i.e.* in the NIR and visible range), covering most of the solar emission spectrum.[6–11] PbS nanocrystals also present a large absorption cross section ($\sim 10^{-15}$ cm^{-2}), long excitonic lifetime ($\sim$200–800 ns), exceptionally high quantum efficiency (80%), and MEG.[12–14]

In view of their technological potential, several PbS quantum dot solar cell (QDSC) architectures have been engineered, ranging from sensitized solar cells that have reached a PCE of 5.6%,[15] to thin films assemblies of QDs, which attained a certified record of 8.5%.[16] Despite these promising results, PbS QDSCs, however, have performed quite disappointingly if we compare them to their dye sensitized counterparts holding a record PCE of 12.3%[17] and the more recent perovskite solar cells with a PCE of 19.3%.[18] The reasons why QDSCs still present low efficiencies have been thoroughly investigated and following facts could be inferred: (a) QDs display localized surface states (trap states) that block the flow of charge carriers into the circuit;[19,20] (b) the interfacial electron injection from the QD to the metal oxide competes with several deleterious fast recombination pathways;[21–24] (c) the polysulphide electrolyte couple employed in sensitized

[a] *Kimika Fakultatea, Euskal Herriko Unibertsitatea (UPV/EHU), and Donostia International Physics Center (DIPC), P. K. 1072, 20080 Donostia, Euskadi, Spain. E-mail: jmkimteo@gmail.com*
[b] *Computational Laboratory for Hybrid/Organic Photovoltaics (CLHYO), Istituto CNR di Scienze e Tecnologie Molecolari (ISTM-CNR), Via Elce di Sotto 8, 06123, Perugia, Italy*
[c] *Institute of Chemistry, The Hebrew University of Jerusalem, Casali Center for Applied Chemistry, 91904, Jerusalem, Israel*
[d] *Department of Theoretical Chemistry, Faculty of Sciences, Vrije Universiteit Amsterdam, De Bolelaan 1081, 1083 HV, Amsterdam, The Netherlands*

† Electronic supplementary information (ESI) available. See DOI: 10.1039/c4cp04976d

QDSCs present a high redox potential that lower the open-circuit voltage and therefore the overall PCE.[25]

In a recent work by Etgar *et al.* on PbS–TiO_2 heterojunction solar cells, the surface of the oxide has been shown to play a crucial role on the performance of the device.[13] In particular, anatase TiO_2 nanosheets exposing a majority of (001) surfaces have been found to generate a higher PCE when compared to standard TiO_2 nanoparticles exposing (101) facets. By attaching PbS QDs of the same size (3.6 nm) on these TiO_2 surfaces with organic linkers, the corresponding solar cells present roughly the same open-circuit voltage, but a significantly different photocurrent: 20.5 mA cm^{-2} for the (001) facets and 16.3 mA cm^{-2} for the (101) facets. The authors briefly suggested that the better photovoltaic performance of the (001) nanosheets might be related to a better adsorption of the PbS QDs on the (001) facets.

Computational modeling provides the opportunity to shed light on these aspects of QDSCs, which are hardly accessible experimentally. However, because modeling QDSCs requires extended systems and poses important challenges, theoretical studies in this type of systems are still scarce.[26,27]

In the present work, we report on the atomistic simulations of PbS QD sensitized TiO_2 solar cells, with the QDs directly adsorbed on the oxide surface.[25] We anticipate that these simulations do not attempt to reproduce exactly Etgar's experiments due to some limitations of our theoretical model. Colloidal QDs are indeed typically metal-rich and the off-stoichiometry is compensated by anionic ligands that dynamically adhere to the QD surface and provide charge neutrality to the entire system. However, the simulation of the ligand-capped PbS QDs, as the ones employed experimentally, represent a serious computational challenge, and only few works have tried to simulate non-stoichiometric systems. A further complication is to model the attachment of metal-rich QDs on TiO_2 with organic linkers. As a consequence of these facts, we decided to model the direct absorption of stoichiometric QDs (without ligands) on the oxide surfaces, paying particular attention to the role of the TiO_2 surface on the electron injection/recombination processes. The model presented in this study can be, however, considered a good approximation to QDs synthesized on metal oxide substrates with *in situ* approaches, such as in SILAR or CBD synthesis, because stoichiometric clusters represent a fair approximation to what is grown on the substrate.

In particular, we demonstrate that the (001) oxide surface binds less strongly with the PbS QD than the (101) facet. In the latter case, the electron injection from the photoexcited QD is faster than into the (001) facet; however, a very fast electron recombination could reduce the overall injection efficiency compared to the (001) surface. Thus, a fast electron injection into the oxide substrate does not always correspond to an efficient electron injection because other recombination pathways should also be taken into account.

Methodology

QD models

Stoichiometric models have been cleaved from the underlying rock-salt structure of bulk PbS. The origin of each model has been set at the center of a $(PbS)_4$ unit and spherical clusters have been sliced out, similar to those obtained by *in situ* approaches. The newly generated models expose non-stoichiometric (111) and stoichiometric (100) facets. Fig. 1 displays the optimized structures of the nanoclusters studied. Some of the models have already been reported in the literature for PbS and PbSe.[26,28–33]

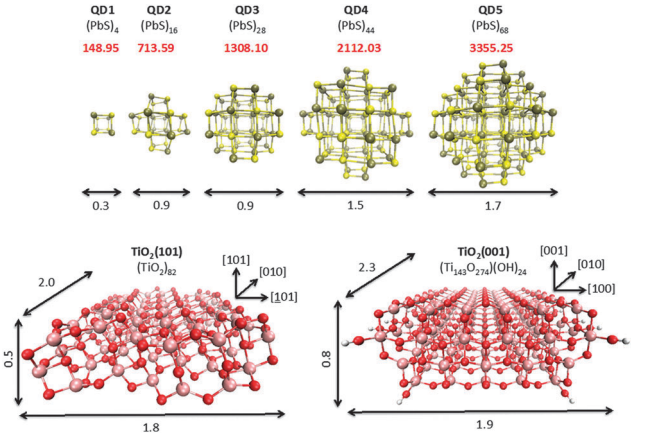

Fig. 1 Optimized geometries of PbS QDs (top) and TiO_2 slab (bottom) models used in this work. Binding energies (red) and size (black) are expressed in kcal mol^{-1} and nm, respectively. Brown = Pb, yellow = S, pink = Ti, and red = O atoms.

TiO_2 models

TiO_2 slab exposing the (101) facet has been built from bulk TiO_2. It is stoichiometric and composed of 82 TiO_2 units; denoted as $(TiO_2)_{82}$ or TiO_2(101) hereafter. The TiO_2 slab exposing the (001) facet is non-stoichiometric and we have added 24 OH^- groups to compensate for the Ti excess of the pristine slab; denoted as $(Ti_{143}O_{274})(OH)_{24}$ or TiO_2(001) hereafter. We opted for cluster models for the TiO_2 surfaces because they allow hybrid DFT calculations and inclusion of solvent effects, mandatory for a proper description of the band edge states of the oxide.[2] Due to the limited size of the oxide slabs, border effects might play a role on the interaction energies. However, the interacting geometries (and therefore the QD–TiO_2 coupling) are less sensitive to these effects. Therefore, the alignment of the electronic levels and the electronic coupling between the solar cell components, which are the key ingredients for the calculation of the injection and recombination rates central to this work, should not be affected.

Computational approach

All the models have been fully optimized without any symmetry constraint with the dispersion corrected (D)[34] Perdew–Burke–Ernzerhof (PBE)[35] xc functional within the Kohn–Sham framework of density functional theory (KS-DFT), as implemented in the ADF 2012.01 software package.[36] For simplicity, geometry optimizations have been carried out *in vacuo* because implicit solvent is shown to play a minor role on the structure of the systems studied (see Fig. S1–S3, ESI†). PbS QDs were relaxed until the maximum norm of the Cartesian gradients was smaller than 1×10^{-3} Hartree $Å^{-1}$. For the QD@TiO_2 nanocomposites,

a looser convergence criterion of 5×10^{-3} Hartree $Å^{-1}$ has been chosen. To take account for relativistic effects, we employed the zero-order regular approximation (ZORA).[37] The choice of the PBE functional to optimize geometries has been followed because it efficiently reproduces the geometry of semiconductor nanostructures at a fraction of the computational cost required by the hybrid functionals.[38–40]

The clusters studied in this work comprise up to 600 atoms; therefore, for some elements the size of the basis-set has been reduced. A double-zeta basis-set (DZ) of Slater-type orbitals (STO) have been added for Pb, S, O, and H atoms, while a single-zeta set (SZ) has been chosen for Ti. In addition, inner lying atomic orbitals (core) have been frozen for all atoms. For some of the PbS models we validated the choice of this basis-set by showing that it fairly reproduces the results obtained with the larger TZP basis-set (see Fig. S4 and S5 in ESI†). We indeed noticed that for the smallest $(PbS)_4$ cluster, increasing the basis-set size from DZ to TZP provoked a shortening of the Pb–S bond distance by about 0.1 Å, while for the larger clusters, the Pb–S bond distance did not augment significantly.

Despite being useful for geometry optimizations and energetics, the PBE, and more in general the GGA functionals, severely underestimate the band-gap of semiconductor nanostructures.[41] Therefore, we decided to use the B3LYP[42] functional in conjunction with the LANL2DZ (Pb and S atoms) and 3-21G* (Ti, O, and H atoms) basis sets, to perform ground and excited state (TD)DFT calculations on the PBE optimized structures. The choice of this functional/basis-set combination has been followed because it reproduces correctly the CB offsets of both TiO_2 and PbS clusters. These calculations have been carried with the Gaussian09 package.[43] To properly describe the electronic structure of the systems studied (see Fig. S2, S3 and S6, ESI†), solvent effects have been included using the conductor-like polarizable continuum model (CPCM) with the water dielectric constants.[44–46]

Radial distribution functions have been calculated using the virtual molecular dynamics (VMD) software.[47] Theoretical UV-Vis curves were obtained using the GAUSSSUM 2.2 program.[48] Charge transfer integrals were computed with a locally developed program.

Results and discussion

1. Bare PbS QDs

Energetics and structure. The binding energy $E_b(n)$[49] of each QD is given as follows:

$$E_b(n) = nE(1) - E(n) \quad (1)$$

where $E(n)$ is the total energy of the composed structure made of n formula units and $E(1)$ is the energy of the smallest unit, *i.e.* $(PbS)_1$. From Fig. 1, all the QD studied here are stable, as shown by the positive binding energies (in red). Moreover, the stability increases with the size of the QD. Our results are in accordance with previous works on II–VI semiconductor nanostructures and predict the crystal growth to be thermodynamically favorable.[49] This process is driven by the minimization of the surface-to-volume ratio with the increasing size of the nanostructure. In this sense, surface ligands, solvent molecules, and the environment play a pivotal role in lowering the surface energy and stabilizing the nanostructure.[40,49–51]

As one may notice from Fig. 1, the optimized PbS QDs preserve the bulk-like structure. However, our models experience a significant distortion upon relaxation (Fig. S3, ESI†). In contrast to II–VI cluster models, where the atomic reconstruction is mainly concentrated on the surface,[39,52] the optimization also affects the core.

To better characterize the optimized models, the Pb–S, Pb–Pb and S–S radial distribution functions (RDF) have been calculated for each QD (see Fig. S7, ESI†). The relaxed models display a broad distribution of Pb–S distances in the range of 2.75–3.75 Å. However, two features are recognizable: (a) a narrow distribution of Pb–S distances corresponding to shortened Pb–S bond lengths, and (b) a wider profile at elongated Pb–S bond distances. Regardless of a particular atomic rearrangement, Pb–S bonds shorten when moving away from the center of the QD (see Fig. S9, ESI†). A lower coordination number on the surface atoms appears to be the driving force for the shrinkage of the bonds in the outer region.[39,52] Concerning Pb–Pb and S–S RDFs, a wide distribution of distances has been found for each model, and the trend is again bimodal. Interestingly, the nearest S–S pairs are closer than the corresponding Pb–Pb pairs. This finding is in contrast with previous works on II–VI QDs, where metal atoms form short M–M contacts.[30,39,40] The Pauli repulsion between the $6s^2$ lone pair in adjacent metal atoms appears to prevent the formation of short Pb–Pb distances.[53]

Electronic structure. Fig. 2 shows the energy of the band edge states for the bare PbS QDs, along with their corresponding density of states (DOS). All the QDs studied display HOMO–LUMO gaps with no mid-gap states, and both HOMO and LUMO are delocalized over each system. QD1 shows the largest band-gap (4.02 eV), which shrinks monotonically with the size of the QD model (2.27 eV in QD5) mainly due to the downward shift of the CB states.

Moving from QD1 to QD5, the DOS becomes denser, as it is evident from the increased curvature at the top of the valence band (VB) and also in the CB. Overall, PbS QDs display a higher density of unoccupied states as compared to II–VI QDs, where the top of the VB is much denser than the bottom of the CB.[39,50,52] As known from the literature and evident here, PbS present a more symmetric DOS, although far from being "mirror-like", with a VB denser than the CB, in agreement with the recent calculations on PbSe QDs.[32]

To get a deeper insight into the electronic structure of PbS QDs, we focused on the QD5 model (~1.7 nm), which closely resembles experimental PbS QDs. As expected, the VB edge spreads *ca.* 4 eV below the HOMO and mainly consists of S 3p orbitals, with a sizeable contribution of Pb 6s and 6p orbitals (Fig. 3a). The CB edge is comprised primarily of Pb 6p states. Localized surface states could act as trap states for the photogenerated electrons and hinder the electron injection to the TiO_2. To unveil the spatial localization of the band edge states, we analyzed the composition of the frontier molecular orbitals.

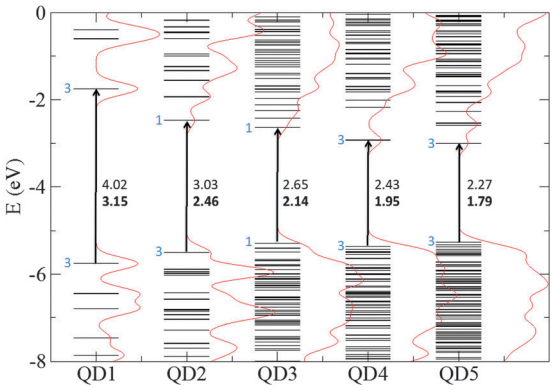

Fig. 2 Energy diagram of the band edge orbitals, along with their corresponding DOS, obtained by a Gaussian convolution of σ = 0.2 eV of the individual orbitals. DOS have been normalized to fit the scale. For each QD, the Kohn–Sham band-gap is provided (in normal style), along with the first TDDFT electronic transition (in bold). Numbers in blue refer to the number of nearly degenerated molecular states at the band edges. Results obtained at the B3LYP/LANL2DZ level.

We found that each atom contributes not more than 7%. Interestingly, as one may notice from Fig. 3b, the high-lying occupied orbitals are mostly spread over the surface, whereas the LUMOs are primarily concentrated on the core, in agreement with results reported for PbSe QDs.[32]

Optical properties. Even if the ground state DFT molecular orbitals deliver fair energy values of the HOMO–LUMO gap, the accurate description of the electronic excitations in these QDs is attained within the more accurate time-dependent TDDFT framework. As shown in Fig. 2, for the smallest QD1 the computed band-gap is 4.02 eV, which has to be compared with the more reasonable TDDFT value of 3.15 eV. This same trend holds for the rest of the models, but with a discrepancy that lowers with the size of the model.

Fig. 4 displays the simulated absorption spectra of the PbS QDs, drawn by a Gaussian convolution of the 10 lowest singlet–singlet TDDFT excitations. With the increasing size of the QD, a significant redshift of the optical spectrum is observed. However, the intensity of the transitions does not appear to follow a clear trend. QD2 displays two strong absorption features, at 2.46 and 2.85 eV. The absorption bands of QD3, QD4, and QD5 appear to be more symmetric and locate at 2.29, 1.97, and 1.82 eV, respectively. This however can be ascribed to the limited number of excited states that we compute.

In our previous work on II–VI QDs, the LUMO was calculated to lie considerably separated from the rest of the CB states such that the lowest electronic excitations were composed from high-lying occupied orbitals to the LUMO. For the PbS models studied here, where a greater number of unoccupied orbitals is available in the excitation window explored, we have found LUMO + n (n = 1–3) to participate (see Table S1, ESI†). Moreover, the lowest-lying TDDFT transitions imply an important mixing of monoelectronic excitations.

2. QD@TiO_2 complexes

To properly simulate PbS QDSC devices, models of realistic size have to be chosen. For this reason, we considered the QD5@TiO_2(101)

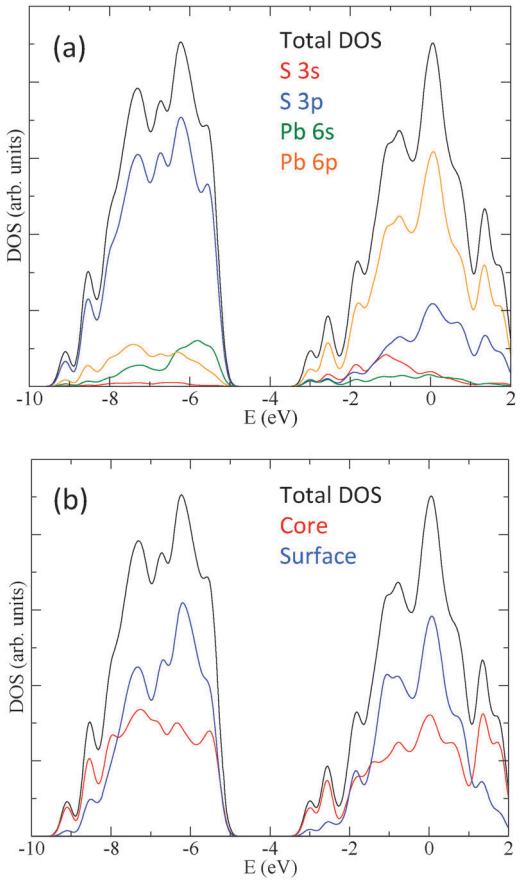

Fig. 3 DOS of the QD5 model, obtained by a Gaussian convolution of σ = 0.2 eV of the individual orbitals, along with the projection into the atomic orbitals (a) and into the core/surface atoms (b). Results obtained at the B3LYP/LANL2DZ level.

and QD5@TiO_2(001) molecular systems. The QD5 moiety presents a calculated first excited state (TDDFT) at 1.79 eV, which is in good agreement with the first experimental band at 1.7 eV.[54,55] The TiO_2(001) and TiO_2(101) slabs have a calculated band-gap (TDDFT) of 3.42 and 3.15 eV, respectively, which match well with the experimental value of 3.2–3.3 eV for standard TiO_2 nanoparticles.[56,57] These benchmark results ensure a fair analysis of the interface between a PbS QD and the metal oxide substrate.

Energetics and structure. The QD5 model exposes Pb-rich (111), S-rich (111), and stoichiometric (100) facets. Consequently, three interaction modes can be envisioned where each of the QD planes faces the TiO_2 slab (see Fig. 5). They are denoted as QD5(Pb-111)@TiO_2, QD5(S-111)@TiO_2, and QD5(100)@TiO_2. In Table 1, the bond energies of the interacting compounds are summarized. To get a deeper insight into the interaction, the bonding energy has been broken down into several terms using the Ziegler and Rauk decomposition scheme.[58–61]

In this framework, the binding energy between two moieties (in our case QD5 and TiO_2) is expressed as follows:

$$\Delta E_{bond} = \Delta E_{prep} + \Delta E_{int} \quad (2)$$

The preparation energy ΔE_{prep} accounts for the energy required to deform the separated fragments from their isolated equilibrium

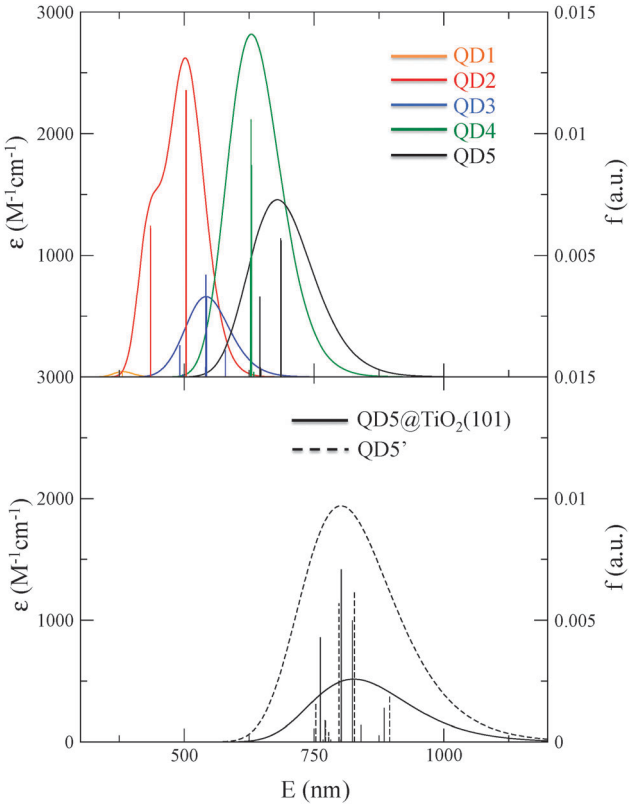

Fig. 4 Simulated absorption spectra of the PbS QDs (top panel) and the QD5@TiO_2(101) interacting complex (bottom panel), drawn by a Gaussian convolution with FWHM = 3000 cm^{-1}, calculated taking into account the lowest 10 electronic transitions. QD5′ refers to the distorted QD, with the geometry it assumes in QD5@TiO_2(101). Results obtained at the B3LYP/LANL2DZ level.

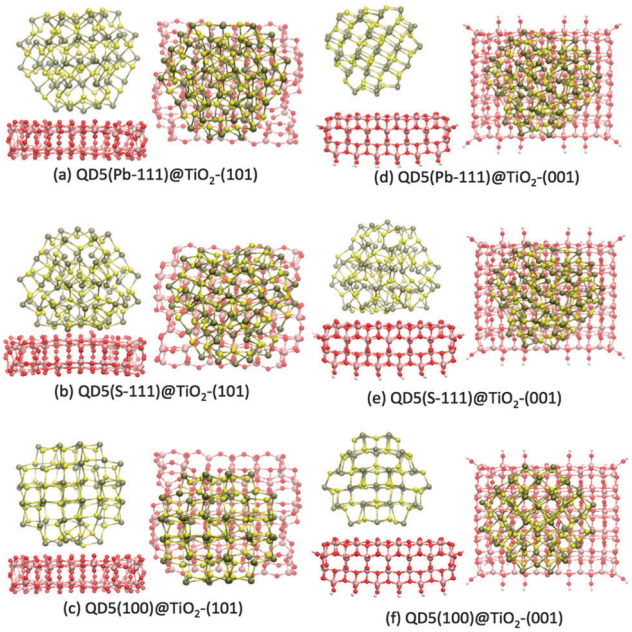

Fig. 5 Side (left) and top (right) views of the optimized geometries of the QD5@TiO_2(101) (a–c) and QD5@TiO_2(001) (d–f) nanocomposites studied.

structure to their geometry in the super-complex (*i.e.* the whole system). The interaction energy ΔE_{int} refers to the instantaneous interaction between the two fragments at the super-complex configuration. This latter term is further decomposed into four contributions with a physical meaning: the Pauli repulsion ΔE_{Pauli}, the electrostatic interaction ΔE_{elst}, the orbital interaction ΔE_{oi} (accounting for charge transfer and polarization effects) and the dispersion (long-range) interaction ΔE_{disp}:

$$\Delta E_{int} = \Delta E_{Pauli} + \Delta E_{elst} + \Delta E_{oi} + \Delta E_{disp} \quad (3)$$

Recall that within this energy decomposition scheme, the attractive and repulsive terms are negative and positive, respectively. Therefore, the more negative the energy term is, the more attractive is the corresponding interaction.

All QD5@TiO_2 models considered here are stable, as shown by the (negative) binding energy ΔE_{bond} between QD5 and TiO_2. The interaction is most likely overestimated for several reasons: (a) the DFT functional employed (*e.g.* pure GGA functionals tend to over bind), (b) the absence of solvent effects, and (c) the limited size of the basis-set. In any case, they provide interesting clues about the QD–TiO_2 interaction.

Contrary to expectations and irrespective of the adsorption mode, the QD5 model is predicted to adsorb more strongly on the TiO_2(101) surface, with binding energies ranging from −85.2 to −187.4 kcal mol^{-1}. When the same QD5 model is adsorbed on the TiO_2(001) facet, the interactions are much weaker, from −13.5 to a maximum (in absolute terms) of −112.5 kcal mol^{-1}. Regardless of the TiO_2 facets, the most stable complex is always obtained when the QD is adsorbed from the S-rich (111) side. Therefore, and unless otherwise stated, the rest of the discussion will focus on this particular adsorption mode.

Inspection of Table 1 shows that the QD5 undergoes a great distortion to enhance the interaction in QD5(S-111)@TiO_2(001), with a huge (destabilizing) preparation energy of 80.3 kcal mol^{-1} *versus* the 54.2 kcal mol^{-1} in QD5(S-111)@TiO_2(001). In addition, irrespective of the oxide facets, the interaction energy ΔE_{int} is mostly electrostatic, covering as much as 54–57% of the attractive terms. The orbital interaction, ΔE_{oi}, contributes with 32%, revealing an important polarization of the electron density of both moieties upon interaction. The QD5 transfers about 0.20 and 0.14 fraction of electrons to the TiO_2(101) and TiO_2(001) nanoparticles, respectively. These polarization effects affect the band edges of both the sensitizer and the oxide, as we will see in the subsequent sections. Finally, the dispersion energy represents about 11–14% of the attractive terms, meaning that even weak interactions may play an important role on defining the conformation of these interfaces, where the contact between the fragments are not very strong overall.

Looking at the geometry of these nanocomposites, there are presumably two types of bonds that are formed at the interface, Pb–O and S–Ti. Correspondingly, we have thus computed the Pb–O and the S–Ti RDFs, as shown in Fig. 6. Irrespective of the slab, the S–Ti bonds are shorter (*ca.* 2.6 Å) and narrowly distributed compared to the Pb–O distances. The binding S(111) facet on the QD, however, undergoes a sizable distortion

Table 1 Energy decomposition analysis of the QD5@TiO_2(101) and QD5@TiO_2(001) complexes, calculated at the D-PBE/SZ(Ti)DZ(H,O,Pb,S). Energies written in kcal mol^{-1}. Values in parentheses give the percentage of each attractive term with respect to the sum of the attractive terms. Q(QD5), given in electrons, indicates the charge developed by the PbS QD5 upon interaction, computed using the Hirshfeld scheme

	QD5(Pb-111)@TiO_2(101)	QD5(S-111)@TiO_2(101)	QD5(100)@TiO_2(101)
ΔE_{bond}	−85.2	−187.4	−71.9
ΔE_{prep}	15.0	150.8	53.7
QD5	5.9	80.3	34.1
TiO_2	9.1	70.5	19.6
ΔE_{int}	−100.2	−338.2	−125.6
ΔE_{Pauli}	200.0	722.1	265.5
ΔE_{elst}	−142.5 (47%)	−605.2 (57%)	−204.3 (52%)
ΔE_{oi}	−96.7 (32%)	−342.9 (32%)	−127.1 (32%)
ΔE_{disp}	61.0 (20%)	−112.2 (11%)	−59.7 (15%)
Q(QD5)	0.0	0.2	−0.1
	QD5(Pb-111)@TiO_2(001)	QD5(S-111)@TiO_2(001)	QD5(100)@TiO_2(001)
ΔE_{bond}	−13.5	−112.5	−52.0
ΔE_{prep}	5.1	128.0	16.7
QD5	5.1	53.8	11.0
TiO_2	0.0	74.1	5.7
ΔE_{int}	−18.7	−240.5	−68.7
ΔE_{Pauli}	1.2	463.4	75.8
ΔE_{elst}	−3.4	−379.1	−67.0
ΔE_{oi}	−2.7	−223.4	−31.3
ΔE_{disp}	−13.7	−101.4	−46.3
Q(QD5)	0.0	0.1	−0.2

upon complexation. It adopts a planar configuration, and the inner Pb atoms move towards the oxide surface driven by attractive O–Pb interactions (either electrostatic or orbital). Pb and O atoms are closer in the QD5(S-111)@TiO_2(101) nanocomposite (2.62 Å) than in the QD5(S-111)@TiO_2(001) (2.90 Å), suggesting that the TiO_2(101) surface indeed better accommodates the QD. The S–Ti bonds are also shorter in the QD5(S-111)@TiO_2(101) complex, even though in this case the difference is rather subtle (2.55 *vs.* 2.57 Å). Consistent with this findings, the integrated Pb–O and S–Ti RDFs reveal a higher coordination between the QD5 and the TiO_2(101) surface.

Electronic structure. Fig. 7 displays the DOS of the QD5(S-111)@TiO_2(101) and QD5(S-111)@TiO_2(001) systems.

Both models show a similar pattern. In brief, the VB of the QD5 isolated fragment, *i.e.*, the high-lying occupied states of the QD, are located about 2.5 eV above the top of the VB of the TiO_2 slab, whereas the unoccupied orbitals are *ca.* 0.3 eV higher in energy than the CB edge of the oxide substrate. This type of staggered alignment, where the unoccupied orbitals of the QD5 are immersed in the manifold of the conduction states of the TiO_2, favors the injection of the photoexcited electron from the QD5 to the oxide. Upon complexation, the QD and the TiO_2 slab undergo a sizeable structural distortion, which affects the position of their band edge states. In particular, the VB edge of QD5 experiences an upward shift and its band-gap reduces by about 0.2–0.3 eV.

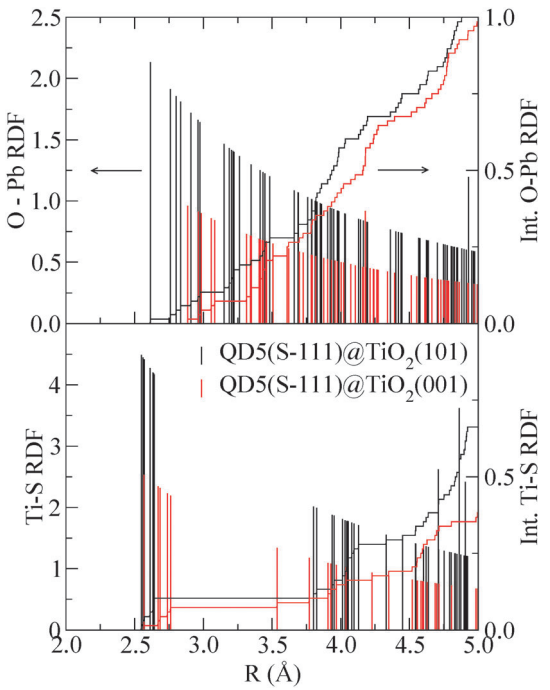

Fig. 6 O–Pb (top panel) and Ti–S (bottom panel) RDF (left axes) of the optimized QD5(S-111)@TiO_2(101) (black) and QD5(S-111)@TiO_2(001) (red) nanocomposites, along with the corresponding integrated RDF (right axes). Geometries obtained at the D-PBE/SZ(Ti)DZ(H,O,Pb,S) level.

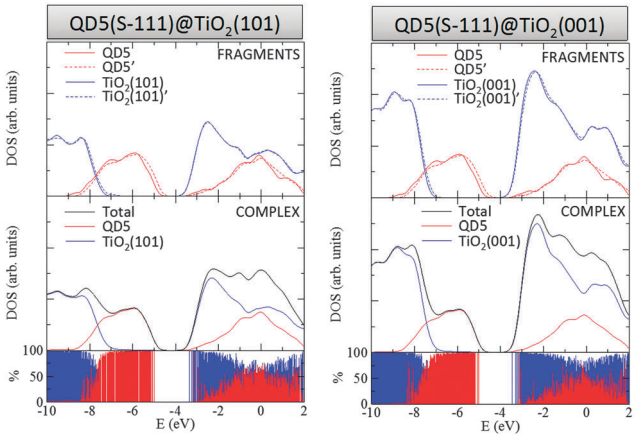

Fig. 7 Top panel: DOS of the PbS QD5 (red) and the TiO_2 (blue) models calculated at their equilibrium geometries (solid lines) and at the structure they have in the interacting complex (dashed lines). Middle panel: DOS of the interacting complex, along with the projection into the QD5 and the TiO_2 fragments. Bottom panel: molecular orbitals of the interacting complex with contributions from the QD5 (red) and the TiO_2 (blue) fragments. The height of the stick represents the % of the orbital localized in each corresponding fragment. Results are obtained at the B3LYP/LANL2DZ level of theory.

The central panel of Fig. 7 depicts the DOS of the interacting complexes, along with the projection into the QD5 and the TiO_2 clusters. The VB and the CB edges of the super-system belong to the QD5 and the TiO_2 slab, respectively. The PDOS essentially agrees with the DOS of the isolated fragments, with a small upward shift of the CB edge of TiO_2 and a downward shift (0.1 eV) of the VB edge of the (distorted) QD.

Finally, in the bottom panel of Fig. 7, we sketched the contribution of the interacting fragments to the super-complex MOs. The high-lying occupied MOs are (almost) pure QD states (red sticks). Deeper in the VB, a notable mixing between QD5 and TiO_2 states is observed. The contribution of QD5 decreases until −8.5 eV, where the MOs are finally localized on the TiO_2 slab. The CB edge belongs mainly to the TiO_2 moiety (blue sticks), but the QD5 states start to appear just above the edge. However, little hybridization between the TiO_2 and the QD states is observed. For example, the LUMO + 5 of the super-complex is fully localized on QD5. The orbital mixing between the nanocrystal and the oxide is crucial in defining the kinetics of electron injection/recombination, as we will see later.

Optical properties. TDDFT calculations have been performed to simulate the optical absorption of the QD5(S-111)@TiO_2(101) model, as seen in Fig. 4 (bottom panel). Compared to the bare QD5′ (*i.e.* QD5 at the geometry of the QD5–TiO_2 complex), the absorption band is red-shifted by *ca.* 0.3 eV (Fig. 9), in agreement with the DOS presented in Fig. 7. Such a spectral displacement, already reported experimentally, has been previously attributed to the redistribution of the electronic density in the interacting complex.[54] Note, however, that the absorption spectra of QD5′ is already red-shifted with respect to QD5, suggesting that the geometrical distortion could also contribute to the experimental bathochromic shift. However, structural effects might not be present in a larger QD, where the reorganization energy is negligible. Overall, the impact of the QD–TiO_2 interaction on the absorption spectrum of the QD is small, suggesting a weak coupling between the QD and the TiO_2 band edge states.

Electron injection and recombination. The main charge transfer process in PbS QDSCs is the electron injection from the photoexcited QD to the CB of the metal oxide semiconductor (Fig. 8).

To shed light on this electron transfer process, we decided to simulate the heterogeneous electron transfer from a single state, d, of the QD to a manifold of acceptor states, k, of the oxide semiconductor. In the weak coupling limit, the rate constant can be expressed according to the Fermi golden rule:

$$k_{\mathrm{d}} = \frac{2\pi}{\hbar}\sum_{\mathrm{k}} |V_{\mathrm{dk}}|^2 \rho(\varepsilon_{\mathrm{d}}) \qquad (4)$$

where $\hbar$ is the Planck's constant, V_{dk} is the electronic coupling between donor and acceptor states, and $\rho(\varepsilon_{\mathrm{d}})$ is the density of states of the oxide substrate evaluated at the donor energy. This approximation is valid as long as the donor state is defined by a single electronic state. At low temperatures, Tisdale *et al.* showed the possibility of hot electron injections from high-lying donor states of PbS QDs.[62,63] At room temperatures, however, the electrons thermally relax to the band edge and inject from the LUMO state. Because PbS QDSCs operate at ambient conditions, we can assume that the donor state is indeed the LUMO of the QD. The electronic coupling elements V_{dk} have been computed by evaluating the off-diagonal elements of the super-system Hamiltonian H projected on the donor (PbS), φ^{d}, and acceptor (TiO_2) states, φ^{k}, of the individual monomers:

$$\langle \varphi^{\mathrm{d}} | H | \varphi^{\mathrm{k}} \rangle \qquad (5)$$

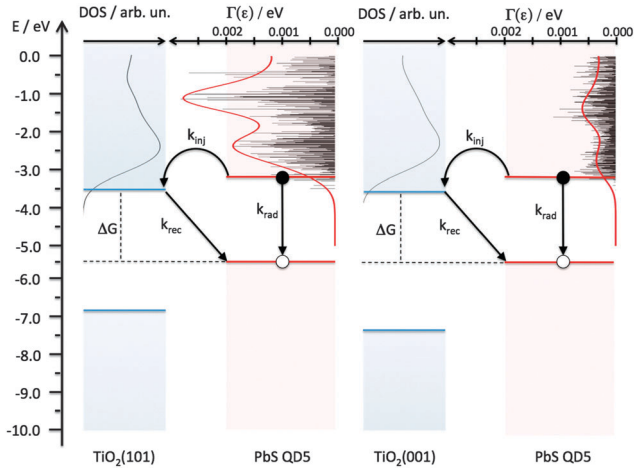

Fig. 8 Scheme of the injection and recombination processes in QD5@TiO_2(101) (left) and QD5@TiO_2(001) (right). For each model, the DOS of the TiO_2 states (blue, left) and the injection function $\Gamma_{\mathrm{inj}}(\varepsilon)$ (red curve, right) are shown, along with the electronic couplings V_{dk} between the d donor state and the manifold of the TiO_2 k acceptor states (black sticks, right). For sake of clarity, the V_{dk} elements have been reduced by a factor of 5. ΔG, calculated as the energy difference between the TiO_2 LUMO and the QD HOMO, represents the driving force for the recombination process.

More details on the approach that we have followed can be found in the literature.[64] The injection rate constant can be alternatively written as follows:

$$k_{\mathrm{d}} = \frac{\Gamma_{\mathrm{inj}}(\varepsilon_{\mathrm{d}})}{\hbar} \tag{6}$$

where $\Gamma_{\mathrm{inj}}(\varepsilon_{\mathrm{d}})$ is the gamma (or injection) function, which provides a visual interpretation of the coupling between the donor and acceptor states as a function of the energy. Evaluation of this term at the donor energy ε_{d} delivers the rate constant, as shown above in eqn (6). In Fig. 8, we depict the electronic couplings between the QD LUMO and the manifold of TiO_2 virtual states, along with the injection function $\Gamma(\varepsilon)$. In the energy range considered, and irrespective of the oxide model, the injection function displays two maxima. The first one appears close to the CB edge of the oxide, where the distribution of the unoccupied TiO_2 states is denser. The second one is centered in the region where the DOS decreases but the coupling of the QD LUMO with the oxide states is stronger.

In Table 2, we have summarized the kinetic parameters of electron injection. The LUMOs of the isolated QDs at the geometry they have in the super-complexes are located at −3.13 and −3.15 eV for the (101) and (001) TiO_2 models, respectively. After interacting with the slab, these energy levels are shifted slightly by 0.02 eV, with values of −3.15 and −3.17 eV, respectively. Although minimal, these new (site) energies will provide a better estimation of the interfacial rate constant.

Comparing the two TiO_2 models, the QD LUMO couples more favorably with the oxide and exposes the (101) facet. This is in agreement with the stronger adsorption interaction of the QD5 on the same surface. The computed injection rates are 1.3 and 2.8 ps for the (101) and (001) oxide slabs, respectively. These values are in qualitative agreement with the recent experiments by Plass and others that pinpoint to interfacial electron transfer from PbS to TiO_2 in the picosecond time scale.[65]

Table 2 Parameters of the injection and recombination processes in QD5@TiO_2(101) and QD5@TiO_2(001): adiabatic and diabatic (site) energies of the frontier orbitals (E and E^{site}, in eV); injection and recombination functions (Γ_{inj} and Γ_{rec}, in eV); injection and recombination rate constants (k_{inj} and k_{rec}, in s^{-1}), injection and recombination rates (τ_{inj} and τ_{rec}, in fs); Franck–Condon factors for the recombination process (FC); and electron injection efficiencies (η_{eff}, in %). All recombination parameters are calculated at ΔG = 0.2 and λ = 0.1 eV

	QD5@TiO_2(101)	QD5@TiO_2(001)
E(HOMO TiO_2)	−6.85	−7.29
E(LUMO TiO_2)	−3.47	−3.54
E^{site}(HOMO PbS)	−5.52	−5.56
E^{site}(LUMO PbS)	−3.15	−3.17
$\Gamma_{\mathrm{inj}}(E^{\mathrm{site}}$(LUMO PbS))	4.90×10^{-4}	2.36×10^{-4}
k_{inj} (s^{-1})	7.44×10^{11}	3.59×10^{11}
τ_{inj} (fs)	1343	2789
Γ_{rec}	2.02×10^{-2}	1.44×10^{-4}
FC(ΔG = 0.2; λ = 0.1)	2.10	2.10
k_{rec} (s^{-1})	6.45×10^{13}	4.59×10^{11}
τ_{rec} (fs)	16	2178
η_{eff}	1	44

At this point, we can finally discuss the expected performance of PbS QDSCs depending on the exposed surface of the oxide slab. The injection efficiency is expressed as follows:

$$\eta_{\mathrm{eff}} = \frac{k_{\mathrm{inj}}}{k_{\mathrm{inj}} + k_{\mathrm{rec}} + k_{\mathrm{rad}}} \tag{7}$$

where k_{inj} is the rate constant for electron injection, k_{rec} is the rate of electron–hole recombination from the injected electron on the surface of TiO_2 back to the hole (HOMO) left on the photoexcited QD, and k_{rad} is the rate constant for radiative emission. The latter occurs in the ns time scale, considerably longer than the time scale of injection and recombination, and therefore it can be safely neglected in the abovementioned expression. The rate of recombination from a manifold of states k (*i.e.* the TiO_2 oxide) to a single acceptor state d (the HOMO of the PbS QD) can be computed as follows:

$$k_{\mathrm{rec}} = \frac{2\pi}{\hbar}\sum_{\mathrm{k}} f(E_{\mathrm{F}}, \varepsilon_{\mathrm{k}}) \cdot |V_{\mathrm{dk}}|^2 \cdot \rho(\varepsilon_{\mathrm{d}}) \cdot \mathrm{FC}(\lambda, \Delta G, \varepsilon_{\mathrm{k}}) \tag{8}$$

where $f(E_{\mathrm{F}},\varepsilon_{\mathrm{k}})$ refers to the Fermi–Dirac distribution, which describes the probability of a given TiO_2 state lying above the quasi-Fermi level (E_{F}) to be occupied, and FC is the Franck–Condon term that in the high temperature limit and harmonic nuclear modes assumes the following form:

$$\mathrm{FC}(\lambda, \Delta G, \varepsilon_{\mathrm{k}}) = \frac{1}{\sqrt{4\pi\lambda k_{\mathrm{B}} T}} \exp\left[\frac{-(\varepsilon_{\mathrm{k}} + \Delta G + \lambda)^2}{4\lambda k_{\mathrm{B}} T}\right] \tag{9}$$

where λ is the reorganization energy, T is the temperature, k_{B} is the Boltzmann constant and ΔG is the energy difference between the donor state k and the acceptor state d. To obtain a qualitative estimate of the k_{rec}, we made some assumptions because some of the variables that are present in these expressions critically depend on the experimental conditions.

(a) The quasi-Fermi level in TiO_2 lies below the CB, but the actual position is unknown and depends on several factors such as the pH of the solution, the electrolyte concentration, and the density of trap states that are on the surface of the oxide. For simplicity and because we would like to provide a qualitative upper limit to the kinetic of charge recombination, we assume that the electron is injected from the CB edge of the TiO_2 (*i.e.* the LUMO). The k_{rec} is then expressed simply by the Marcus formula:

$$\begin{aligned} k_{\mathrm{rec}} &= \frac{2\pi}{\hbar}|V_{\mathrm{dk}}|^2 \frac{1}{\sqrt{4\pi\lambda k_{\mathrm{B}} T}} \exp\left[\frac{-(\Delta G + \lambda)^2}{4\lambda k_{\mathrm{B}} T}\right] \\ &= \frac{\Gamma_{\mathrm{rec}}}{\hbar} \cdot \mathrm{FC}(\lambda, \Delta G) \end{aligned} \tag{10}$$

(b) The reorganization energy is the energy required by donor and acceptor (and the solvent that surrounds them) to rearrange their geometries upon electron transfer. Usually, this value can be estimated from calculations; however, the cluster models of the QDs in this work are rather small and present strong quantum confinement effects. These QDs lead to unrealistically large reorganization energies (>0.5 eV) that experimentally are estimated to be around 0.1 eV or even smaller.[63] Therefore,

we decided to vary this term parametrically between 0.01 and 0.50 eV and look at its effect on the injection efficiency.

(c) ΔG is the energy difference between the donor state k and the acceptor state d. Just considering the simple energy difference LUMO(TiO_2)–HOMO(PbS), the ΔG is about 1.4 eV, which is considerably larger than the reorganization energy. According to the Marcus theory, the kinetics of electron transfer would then fall in the inverted regime and the electron–hole recombination would be virtually forbidden. In reality, TiO_2 presents defect states that could promote the back electron transfer to the QD by decreasing the energy gap with the sensitizer HOMO. This justification has already been proposed to explain the fast recombination rates in DSSCs, which would otherwise be unaccountable. The situation is even more involved for QD sensitizers because they also develop localized states on their surface, which could act as traps for the photo-generated holes. For simplicity, we employ non-defective clusters to reproduce both the sensitizer and the oxide substrate. However, to model the role of the surface effects on the recombination mechanism, we decided to tune the ΔG term parametrically and see how this would affect the electron injection efficiency.

Regarding points (b) and (c) above, we must point out that both TiO_2 slabs present practically the same DOS for the metal oxide and the same structure and energetics of the QD absorbed on the surface. This leads to same ΔG and λ values for both oxide surfaces, and thus the same FC factors. This is important because the difference between the rates of recombination with the (101) and (001) slabs lie only on the electronic coupling, or Γ_{rec}, which we can evaluate directly from the calculations.

In Fig. 9, we present the electron injection efficiency computed with formula (7), by changing parametrically $k_{rec}(\lambda,\Delta G)$. As it is immediately clear, in general, the injection efficiency increases with ΔG because for $\Delta G > \lambda$, the recombination process enters in the inverted Marcus region, and it is therefore slowed down. $\lambda = 0.5$ eV represents an exception to the rule, but as stated earlier, experimental reorganization energies lie considerably below such a large value. Importantly, and irrespective of λ, the (001) facet delivers higher injection efficiencies. The inspection of Table 2 provides more details on why (001) is more efficient. The injection rate k_{inj} from the PbS to the (101) facets is about twice as large as the (001) because of a larger Γ_{inj}. At the same time, the recombination rate k_{rec} from the (101) is about 100 times faster, as a consequence of a very efficient electronic coupling of the LUMO of TiO_2(101) with the HOMO of the QD. Therefore, the gain obtained by injecting the photoexcited electron faster in (101) is inhibited by a very fast electron–hole recombination, which drastically reduces the overall efficiency. On the other hand, the (001) slab slowly injects the electrons but the less favorable coupling for the electron recombination provides overall larger injection efficiencies.

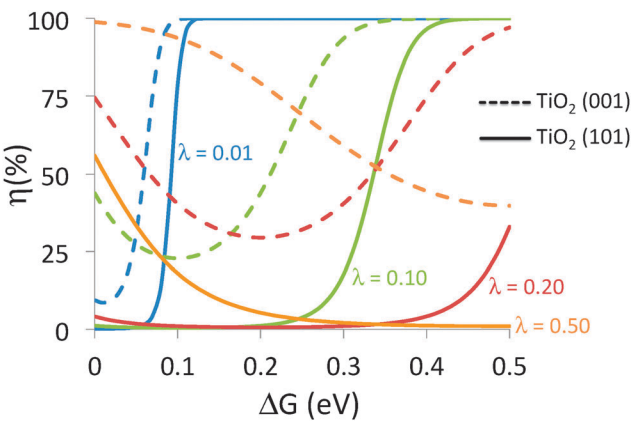

Fig. 9 Electron injection efficiency for the QD5@TiO_2(101) (solid curves) and QD5@TiO_2(001) (dashed curve) as a function of ΔG, calculated for various λ.

Future perspectives and conclusion

In this work, we provide atomistic simulations based on DFT to explain the physico-chemical processes occurring at the interface between PbS QDs and oxide semiconductors of different morphologies. We show that a bare QD model injects photoexcited electrons more efficiently into the TiO_2 slabs exposing (001) facets. This result is in qualitative agreement with the experimental measurement carried out by Etgar *et al.* However, we must warn that this agreement might be unintentional because the PbS QDs employed in the experiments are linked to the surface of the oxide nanoparticles with mercaptopropionic acid ligands that are not included in our model. The effect of these ligands on different surfaces is unpredictable at this time and might be crucial for a correct interpretation of the experimental data. We are currently working to address this issue.

On the other hand, our model could be used as a litmus test to analyze the effect of QDs directly grown on the oxide interface, as it is done in the SILAR process.[25] Here, the QD directly is synthesized on the surface with a layer-by-layer deposition and without the help of linkers. Because our model shows a better adsorption from the side of sulfur atoms, we expect that our calculations could provide reasonable results in the case that the nucleation of the QD begins by dipping the TiO_2 nanoparticles in a solution of sulfur precursors.

Acknowledgements

This research was funded by Eusko Jaurlaritza/Basque Government (IT588-13 and S-PC12UN003) and the Spanish Office for Scientific Research (CTQ2012-38496-C05-01). The SGI/IZO-SGIker UPV/EHU is gratefully acknowledged for the generous allocation of computational resources. JMA would like to thank the Spanish Ministry of Education for funding through a FPU fellowship (AP2009-1514). FDA thanks FP7-ENERGY-2010 project "ESCORT"(261920) and CNR-EFOR for financial support.

Notes and references

1 B. O'Regan and M. Grätzel, *Nature*, 1991, **353**, 737–740.
2 M. Pastore, S. Fantacci and F. De Angelis, *J. Phys. Chem. C*, 2013, **117**, 3685–3700.
3 A. P. Alivisatos, *J. Phys. Chem.*, 1996, **100**, 13226–13239.

4 A. P. Alivisatos, *Science*, 1996, **271**, 933–937.
5 W. Shockley and H. J. Queisser, *J. Appl. Phys.*, 1961, **32**, 510–519.
6 R. Reiche, R. Thielsch, S. Oswald and K. Wetzig, *J. Electron Spectrosc. Relat. Phenom.*, 1999, **104**, 131–149.
7 Z. Zeng, S. Wang and S. Yang, *Chem. Mater.*, 1999, **11**, 3365–3369.
8 K. K. Nanda and S. N. Sahu, *Adv. Mater.*, 2001, **13**, 280–283.
9 M. Kowshik, W. Vogel, J. Urban, S. K. Kulkarni and K. M. Paknikar, *Adv. Mater.*, 2002, **14**, 815–818.
10 Y. Zhou, H. Itoh, T. Uemura, K. Naka and Y. Chujo, *Langmuir*, 2002, **18**, 5287–5292.
11 S. Wu, H. Zeng and Z. A. Schelly, *Langmuir*, 2005, **21**, 686–691.
12 L. Etgar, J. Park, C. Barolo, M. K. Nazeeruddin, G. Viscardi and M. Graetzel, *ACS Appl. Mater. Interfaces*, 2011, **3**, 3264–3267.
13 L. Etgar, W. Zhang, S. Gabriel, S. G. Hickey, M. K. Nazeeruddin, A. Eychmüller, B. Liu and M. Grätzel, *Adv. Mater.*, 2012, **24**, 2202–2206.
14 L. Etgar, T. Moehl, S. Gabriel, S. G. Hickey, A. Eychmüller and M. Grätzel, *ACS Nano*, 2012, **6**, 3092–3099.
15 J.-W. Lee, D.-Y. Son, T. K. Ahn, H.-W. Shin, I. Y. Kim, S.-J. Hwang, M. J. Ko, S. Sul, H. Han and N.-G. Park, *Sci. Rep.*, 2013, **3**, 1050.
16 C.-H. M. Chuang, P. R. Brown, V. Bulović and M. G. Bawendi, *Nat. Mater.*, 2014, **13**, 796–801.
17 A. Yella, H.-W. Lee, H. N. Tsao, C. Yi, A. K. Chandiran, M. K. Nazeeruddin, E. W.-G. Diau, C.-Y. Yeh, S. M. Zakeeruddin and M. Grätzel, *Science*, 2011, **334**, 629–634.
18 H. Zhou, Q. Chen, G. Li, S. Luo, T.-b. Song, H.-S. Duan, Z. Hong, J. You, Y. Liu and Y. Yang, *Science*, 2014, **345**, 542–546.
19 O. Voznyy, S. M. Thon, A. H. Ip and E. H. Sargent, *J. Phys. Chem. Lett.*, 2013, **4**, 987–992.
20 O. Voznyy, D. Zhitomirsky, P. Stadler, Z. Ning, S. Hoogland and E. H. Sargent, *ACS Nano*, 2012, **6**, 8448–8455.
21 I. Hod, V. Gonz, Z. Tachan, F. Fabregat-santiago, J. Bisquert and A. Zaban, *J. Phys. Chem. Lett.*, 2011, **2**, 3032–3035.
22 I. Mora-Seró, D. Gross, T. Mittereder, A. a. Lutich, A. S. Susha, T. Dittrich, A. Belaidi, R. Caballero, F. Langa, J. Bisquert and A. L. Rogach, *Small*, 2010, **6**, 221–225.
23 H. Choi, M. Kuno, G. V. Hartland and P. V. Kamat, *J. Mater. Chem. A*, 2013, **1**, 5487–5491.
24 M. Planells, L. X. Reynolds, U. Bansode, S. Chhatre, S. Ogale, N. Robertson and S. A. Haque, *Phys. Chem. Chem. Phys.*, 2013, **15**, 7679–7684.
25 H. Lee, H. C. Leventis, S.-J. Moon, P. Chen, S. Ito, S. A. Haque, T. Torres, F. Nüesch, T. Geiger, S. M. Zakeeruddin, M. Grätzel and M. K. Nazeeruddin, *Adv. Funct. Mater.*, 2009, **19**, 2735–2742.
26 R. Long and O. V. Prezhdo, *J. Am. Chem. Soc.*, 2011, **133**, 19240–19249.
27 D. N. Tafen, R. Long and O. V. Prezhdo, *Nano Lett.*, 2014, **14**, 1790–1796.
28 J. He, C. Liu, F. Li, R. Sa and K. Wu, *Chem. Phys. Lett.*, 2008, **457**, 163–168.
29 P. Koirala, B. Kiran, A. K. Kandalam, C. A. Fancher, H. L. de Clercq, X. Li and K. H. Bowen, *J. Chem. Phys.*, 2011, **135**, 134311.
30 H. Zeng, Z. A. Schelly, K. Ueno-Noto and D. S. Marynick, *J. Phys. Chem. A*, 2005, **109**, 1616–1620.
31 S. V. Kilina, C. F. Craig, D. S. Kilin and O. V. Prezhdo, *J. Phys. Chem. C*, 2007, **111**, 4871–4878.
32 A. Franceschetti, *Phys. Rev. B: Condens. Matter Mater. Phys.*, 2008, **78**, 075418.
33 S. V. Kilina, D. S. Kilin and O. V. Prezhdo, *ACS Nano*, 2009, **3**, 93–99.
34 S. Grimme, J. Antony, S. Ehrlich and H. Krieg, *J. Chem. Phys.*, 2010, **132**, 154104.
35 J. P. Perdew, K. Burke and M. Ernzerhof, *Phys. Rev. Lett.*, 1996, **77**, 3865–3868.
36 G. te Velde, F. M. Bickelhaupt, E. J. Baerends, C. F. Guerra, S. J. A. van Gisbergen, J. G. Snijders and T. Ziegler, *J. Comput. Chem.*, 2001, **22**, 931–967.
37 E. van Lenthe, A. Ehlers and E.-J. Baerends, *J. Chem. Phys.*, 1999, **110**, 8943–8953.
38 F. De Angelis and L. Armelao, *Phys. Chem. Chem. Phys.*, 2011, **13**, 467–475.
39 J. M. Azpiroz, E. Mosconi and F. D. Angelis, *J. Phys. Chem. C*, 2011, **115**, 25219–25226.
40 J. M. Azpiroz, X. Lopez, J. M. Ugalde and I. Infante, *J. Phys. Chem. C*, 2012, **116**, 2740–2750.
41 J. M. Azpiroz, J. M. Ugalde and I. Infante, *J. Chem. Theory Comput.*, 2014, **10**, 76–89.
42 A. D. Becke, *J. Chem. Phys.*, 1993, **98**, 1372–1377.
43 M. J. Frisch, G. W. Trucks, H. B. Schlegel, G. E. Scuseria, M. A. Robb, J. R. Cheeseman, G. Scalmani, V. Barone, B. Mennucci, G. A. Petersson, H. Nakatsuji, M. Caricato, X. Li, H. P. Hratchian, A. F. Izmaylov, J. Bloino, G. Zheng, J. L. Sonnenberg, M. Hada, M. Ehara, K. Toyota, R. Fukuda, J. Hasegawa, M. Ishida, T. Nakajima, Y. Honda, O. Kitao, H. Nakai, T. Vreven, J. A. Montgomery Jr., J. E. Peralta, F. Ogliaro, M. Bearpark, J. J. Heyd, E. Brothers, K. N. Kudin, V. N. Staroverov, R. Kobayashi, J. Normand, K. Raghavachari, A. Rendell, J. C. Burant, S. S. Iyengar, J. Tomasi, M. Cossi, N. Rega, J. M. Millam, M. Klene, J. E. Knox, J. B. Cross, V. Bakken, C. Adamo, J. Jaramillo, R. Gomperts, R. E. Stratmann, O. Yazyev, A. J. Austin, R. Cammi, C. Pomelli, J. W. Ochterski, R. L. Martin, K. Morokuma, V. G. Zakrzewski, G. A. Voth, P. Salvador, J. J. Dannenberg, S. Dapprich, A. D. Daniels, Ö. Farkas, J. B. Foresman, J. V. Ortiz, J. Cioslowski and D. J. Fox, *Gaussian 09 Revision B.01*, 2009.
44 M. Cossi and V. Barone, *J. Phys. Chem. A*, 2000, **104**, 10614–10622.
45 M. Cossi and V. Barone, *J. Chem. Phys.*, 2001, **115**, 4708–4717.
46 M. Cossi, N. Rega, G. Scalmani and V. Barone, *J. Comput. Chem.*, 2003, **24**, 669–681.
47 W. Humphrey, A. Dalke and K. Schulten, *J. Mol. Graphics*, 1996, **14**, 33–38.
48 N. M. O'Boyle, A. L. Tenderholt and K. M. Langner, *J. Comput. Chem.*, 2007, **29**, 839–845.

49 C. R. A. Catlow, S. T. Bromley, S. Hamad, M. Mora-Fonz, A. A. Sokol and S. M. Woodley, *Phys. Chem. Chem. Phys.*, 2010, **12**, 786–811.
50 J. M. Azpiroz, J. M. Matxain, I. Infante, X. Lopez and J. M. Ugalde, *Phys. Chem. Chem. Phys.*, 2013, **15**, 10996–11005.
51 J. M. Azpiroz, E. Mosconi, J. M. Ugalde and F. D. Angelis, *J. Phys. Chem. C*, 2014, **118**, 3274–3284.
52 J. M. Azpiroz, I. Infante, X. Lopez, J. M. Ugalde and F. De Angelis, *J. Mater. Chem.*, 2012, **22**, 21453–21465.
53 C. S. S. Sandeep, J. M. Azpiroz, W. H. Evers, S. C. Boehme, I. Moreels, S. Kinge, L. D. A. Siebbeles, I. Infante and A. J. Houtepen, *ACS Nano*, 2014, **8**, 11499–11511.
54 B.-r. Hyun, Y.-w. Zhong, A. C. Bartnik, L. Sun, H. D. Abrun, F. W. Wise, J. D. Goodreau, J. R. Matthews, T. M. Leslie and N. F. Borrelli, *ACS Nano*, 2008, **2**, 2206–2212.
55 A. H. Khan, U. Thupakula, A. Dalui, S. Maji, A. Debangshi and S. Acharya, *J. Phys. Chem. C*, 2013, **117**, 7934–7939.
56 M. Khoudiakov, A. R. Parise and B. S. Brunschwig, *J. Am. Chem. Soc.*, 2003, **125**, 4637–4642.
57 Y.-X. Weng, Y.-Q. Wang, J. B. Asbury, H. N. Ghosh and T. Lian, *J. Phys. Chem. B*, 2000, **104**, 93–104.
58 T. Ziegler and A. Rauk, *Theor. Chim. Acta*, 1977, **46**, 1–10.
59 T. Ziegler and A. Rauk, *Inorg. Chem.*, 1979, **18**, 1558–1565.
60 T. Ziegler and A. Rauk, *Inorg. Chem.*, 1979, **18**, 1755–1759.
61 K. Kitaura and K. Morokuma, *Int. J. Quantum Chem.*, 1976, **10**, 325–340.
62 W. A. Tisdale, K. J. Williams, B. A. Timp, D. J. Norris, E. S. Aydil and X.-Y. Zhu, *Science*, 2010, **328**, 1543–1547.
63 W. A. Tisdale and X.-Y. Zhu, *Proc. Natl. Acad. Sci. U. S. A.*, 2011, **108**, 965–970.
64 E. Ronca, G. Marotta, M. Pastore and F. De Angelis, *J. Phys. Chem. C*, 2014, **118**, 16927–16940.
65 R. Plass, S. Pelet, J. Krueger and M. Gra, *J. Phys. Chem. B*, 2002, **106**, 7578–7580.

